applied sciences

MDPI

Article

Topology and Response Surface Optimization of a Bicycle Crank Arm with Multiple Load Cases

Ahmad Yusuf Ismail, Gangta Na and Bonyong Koo *

Department of Mechanical Engineering, Kunsan National University, Gunsan, Jeollabuk-do 54150, Korea; yusuf@itats.ac.id (A.Y.I.); zooy3405@naver.com (G.N.)

* Correspondence: bykoo@kunsan.ac.kr; Tel.: +82-63-469-4713

Received: 24 February 2020; Accepted: 23 March 2020; Published: 24 March 2020

Abstract: This paper presents an application of topology optimization and response surface method to optimize the geometry of a bicycle crank arm and the experimental validation of it. This is purposely to reduce the crank arm mass and create a preliminary design of a lightweight structure necessary for the high-performance bicycle development. A three-dimensional bike crank arm model was made in the SpaceClaim software followed by a static finite element analysis using ANSYS Workbench 2019 R1. A multiple cycling load was applied simultaneously in seven crank angles of 30, 45, 60, 90, 120, 135, and 150° relative to the horizontal position to create the multiple loads to the crank. From there, topology optimization was then conducted to investigate the effect of mass constraint, stress constraint, angle of cycling, and crank materials on the topological pattern result. To minimize stress concentration at corners, a shape optimization using the response surface method was conducted and obtained the final geometry. From the result, it is shown that both optimization methods not only successfully reduce the crank arm mass and provide several optimum design options but also are able to reduce the maximum stress in the crank arm up to 20% after the optimization process. The experimental validation using a newly developed wireless measurement system shows a considerable agreement to the numerical results.

Keywords: topology optimization; response surface method; multiple loads; bicycle crank arm

1. Introduction

Since the oil and energy consumption issues have been rapidly arising during past decades, a non-fuel based vehicle such as the bicycle has been shifting people's preference. From the bike-to-work campaign up to the behavioral psychology study of the cyclist [1], cycling has apparently been part of people's common lifestyle ever since the 1900s. From the environmental side, cycling is also one of the best solutions to reduce the global warming issue. Recently, the South Korean government has initiated an effort to slash the greenhouse emissions by enforcing cycling as a transportation method instead of driving a car or motorcycle, as reported by The Korea Transport Institute (KOTI) [2]. This makes the bicycle become a more interesting topic for scientists, researchers, and even an international standardization body such as the International Standard Organization (ISO) [3].

One of the most important aspects that make a bicycle interesting for people, is the bicycle design. A design, besides being a matter of aesthetics, relates closely to the ergonomic of mechanical structure and even structural reliability [4,5]. A good design will not only make human–machine interaction become better but also makes the machine itself more reliable and have a longer period of usage.

A lightweight structure has been one of the biggest long-time challenges in the structural engineering industry since it relates closely to the structural performance, reliability, as well as manufacturing cost. This lighter structure has also made the bicycle design evolve since the past

years. Bicycle manufacturers compete with each other to find a better production process and use several optimization methods to create lighter products without losing their performance. For instance, in the world of racing bikes, a lighter material means a big opportunity to reach faster speed in the competition. That is why several researchers have published their ideas to optimize and create a better bicycle component, i.e., the crank arm and pedal, as shown by several published patents [6–8].

Topology optimization is a well-known method in the design optimization process as has been discussed by researchers in terms of pursuing a lightweight structure [9]. It is a very powerful method to reduce the weight of a component without losing its best performance. Yang et al. [10] investigate the stress-constrained topology optimization based on maximum stress measures that give beneficial information about an easy implementation, low computational cost, and stable converge topology optimization process. Viviani et al. [11] use multi-objective structural topology optimization for turbine brake pads subject to thermal and brake vibration. The result of the study shows that the optimized structure meets the stiffness requirement, as well as improves vibration performance. In a similar application, the same method has also been used to optimize the bucket foundation design of offshore wind turbines [12]. Slavov and Bakalova [13] manage to optimize the weight of gearbox housing elements using topology optimization techniques. It provides potential directions for further gearbox housing development, as well.

Topology optimization has also been used for improving spacecraft design for years. A study by Orme et al. [14] utilize additive manufacturing and topology optimization to develop space flight hardware. The additive manufacturing constraints include the minimization of support structures and heat transfer jumps that can cause artifact warpage. The result shows that the proposed new optimized model is suitable for the respective missions. Meanwhile, Qu et al. [15] implement a multi-objective topology optimization for a large-aperture space mirror. The optimized design is found to be very effective as a lightweight primary mirror assembly.

In other applications, Sleesongsom and Bureerat [16] apply a topology optimization method using multi-objective population-based incremental learning and multigrid ground element. It is found that the proposed optimization method shows superiority over other techniques. This method is also found to be effective in the telecommunication field as Frascolla et al. use this method to optimize the C-RAN backhaul design [17]. Tauzowksi et al. [18] propose a novel approach of functor-oriented topology optimization of elastoplastic structures. Several other studies also state that this method is very useful to create lighter components in precision engineering [19], composite material [20], and civil engineering application [21,22].

Nevertheless, a study on the application of topology optimization on the bicycle crank arm seems to be lacking. It is very important since the crank arm plays a major role in the bicycle component. It is the part where the cycling force is first applied before transmitting into the frame. Most of the research was only focused on the force evaluation or stress distribution on the crank and seldom discussed how to improve the crank arm design. One good approach has been done by McEwen et al. [23] where a complete study on the design and manufacture of a bike crank arm is presented in which the topology optimization procedure is included. This paper, therefore, extends the approach of using topology optimization on a bicycle crank arm with an additional application of a response surface optimization method to gain a better improved optimized design. The additional response surface method is used to reduce stress concentrations after the optimized topology has been obtained. Finally, the optimized design is experimentally validated.

2. Methods

In general, the research methodology is shown in the flowchart in Figure 1. It is started by reviewing all the works of literature related to bike crank arm researches and followed by creating a three-dimensional model in SpaceClaim and ANSYS Workbench 19.1. It is then followed by executing the topology optimization procedure with several variation studies. From the result, a response surface optimization method is applied to improve the stress performance result by

topology optimization. Finally, an experimental measurement using the 3D printing sample is conducted to validate the numerical result. Each part of the flow is explained in more detail in the following subsection.

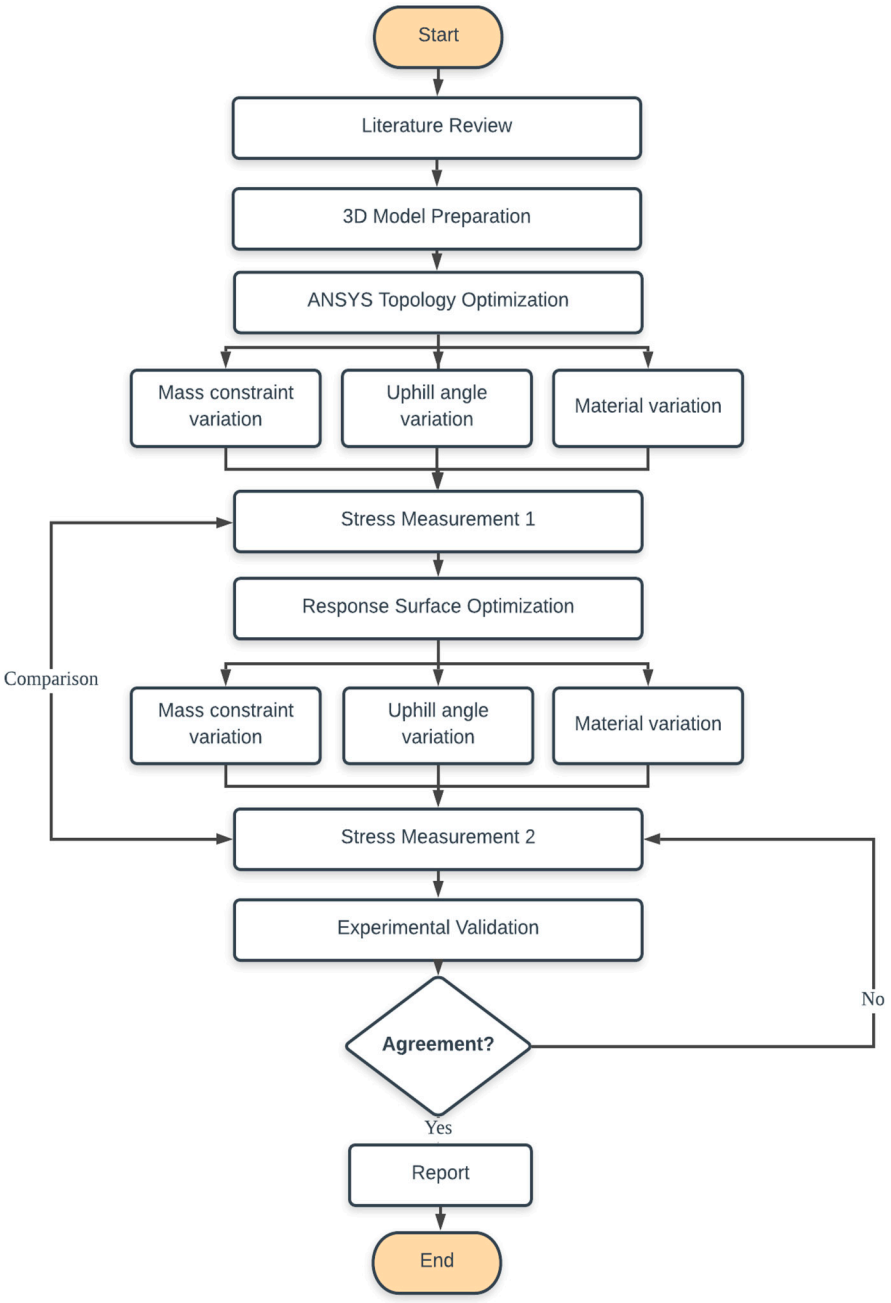

Figure 1. Flowchart of the research.

2.1. Models

A three-dimensional aluminum alloy model of the bike crank arm is made in the SpaceClaim ANSYS Workbench 2019 R1, as seen in Figure 2. The geometry of the used model is the typical geometry of the commercial bike crank arm. The crankshaft hole is designed with a 19.78 mm diameter hole while the pedal hole is designed with a 12.8 mm diameter hole. The distance between the crankshaft and pedal spindle holes is set to be 175 mm, similar to that of McEwen et al. [23]. Meanwhile, the arm thickness is designed to be 12.5 mm.

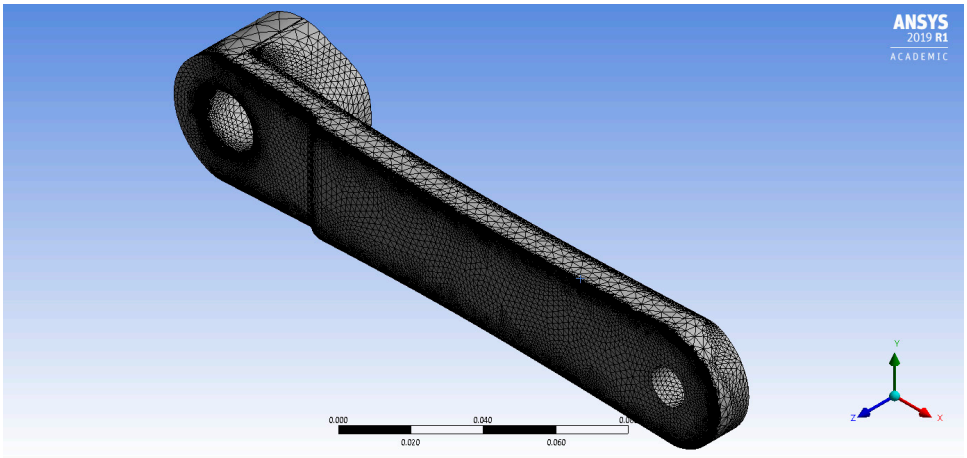

Figure 2. Bicycle crank arm model.

A mesh discretization and refinement strategy have been generated in the ANSYS Workbench environment. Up to three levels of mesh refinement are applied at particular locations, i.e., the bottom crankshaft and top pedal hole purposely to obtain more accurate results. As mentioned in the previous section, these locations are very important as the place where the force is first applied (pedal hole) and transferred (crankshaft hole). The mesh refinement is also made in the crank body to provide sufficient discretization for topology optimization purposes. From the mesh resolution setting, the model has 967,769 nodes and 677,089 elements in total. The initial mass of this model is 0.30 kg.

A static finite element analysis (FE) is conducted with multiple forces in various angles from 30 to 150°, as seen in Figure 3. These various angles are selected to represent the distribution of pedaling load as investigated by McEwen et al. [23] where the crank angle can also be drawn as the force angle at the pedal in the figure. These forces also simultaneously create a moment on the crank arm which is also known as the effective force F_p as given by Casas et al. [24]. According to Hung et al. [25] and Hung and Lim [26], this kind of force is generated from the equation of motion of bicycle dynamics (see Figure 4).

$$T_{chain} = T_{pedal} \tag{1}$$

where T is the torque at both the pedal and chain. From Newton's third law of force balance, the torque generated from effective pedaling force $F\neg_p$ has the same value with the torque generated at the chain, which is also known as the cycling force transmission from the cycling force to the chain force, i.e., tire rotation in the rear wheel. Therefore, this torque balance can also be written in the form of force balance as:

$$F_{ch}R_s = F_pL_p \cos\theta_p \tag{2}$$

where F_{ch} is the force at the chain, R_s is the sprocket radius, $F\neg_p$ is the effective cycling force (which is the multiple loads used in this paper), and L_p is the radius of the cycling force or simply, the crank arm length. The distribution of the effective force F_p, as mentioned before, is depicted in Figure 5 below.

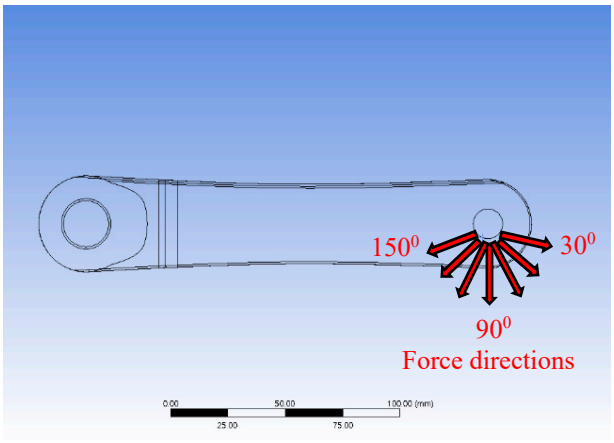

Figure 3. Multiple forces with various angles.

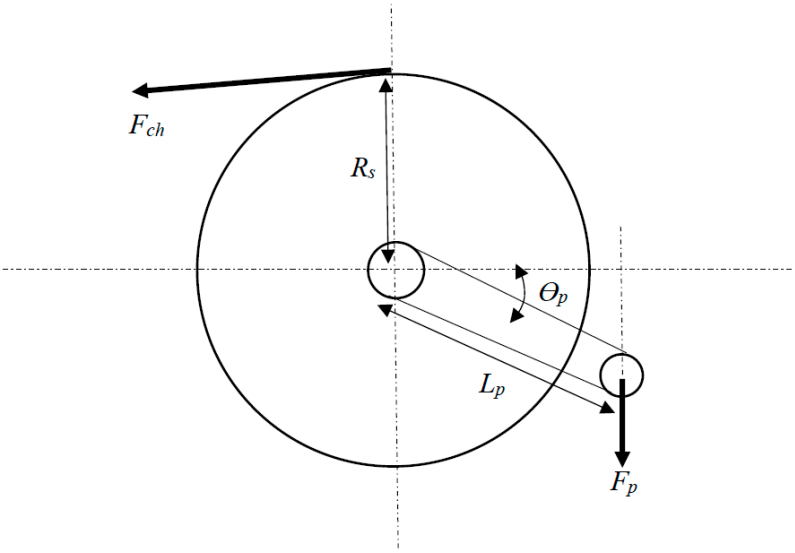

Figure 4. Cycling dynamics.

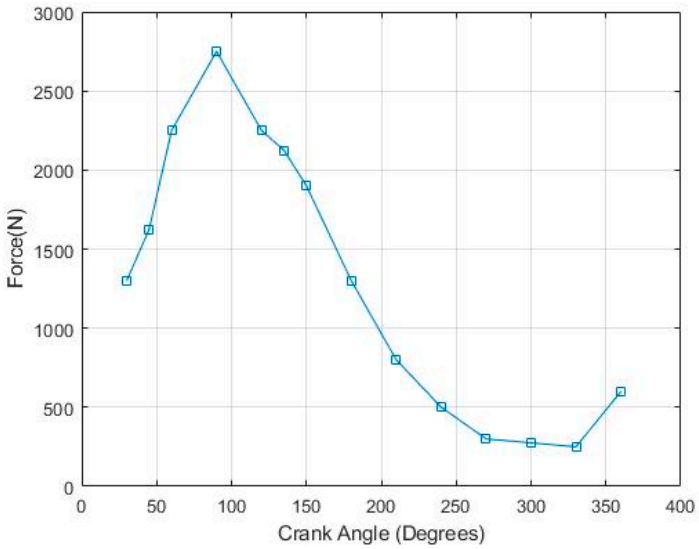

Figure 5. Force distribution along the pedaling cycle (re-drawn using results in [23]).

2.2. Topology Optimization Method

Based on the force distribution described before, an assumption is made for the optimization process. To model the dynamic multiple cycling loads on the crank, as seen in Figures 3 and 5, a combination of seven loads is considered. Each load represents the cycling load at each angle. In this case, seven maximum forces from 30 to 150° crank angles are used. Table 1 lists all the load distribution:

Table 1. Load distribution for topology optimization.

Crank angle	30°	45°	60°	90°	120°	135°	150°
Force (N)	1300	1625	2250	2750	2250	2125	1900

From these load distributions, two scenarios of topology optimization are investigated, i.e., compliance minimization with mass constraint and mass minimization with stress constraint purposely to accommodate the effect of mass constraint, uphill angle, stress constraint, and materials. In turn, this will give a broader range of optimized crank arm design. Each scenario is described in the following subsection.

2.2.1. Effect of Mass Constraint

The objective function for this scenario is the compliance minimization with several mass constraint variation which can be written as the following equation:

$$\min \sum F_{pi}^{T} u_i \tag{3}$$

Such that:

1. $m_{opt} \leq 0.3 m_0$
2. $m_{opt} \leq 0.4 m_0$
3. $m_{opt} \leq 0.5 m_0$
4. $m_{opt} \leq 0.6 m_0$

where i indicates the multiple force sequence (i = 1, 2, 3 ... 7), $F\neg_p$ is the applied force and u_i is the displacement, m_0 is the initial mass and m_{opt} is the optimized mass.

The five mass constraints for topology optimization is set from 30% to 60%. This percentage is a general approximation for optimization and explains the optimization history. Then, using ANSYS Workbench 2019 R1 topology optimization, the optimized designs are generated. After that, a curve fitting in the Space Claim is used to obtain the final design.

2.2.2. Effect of Stress Constraint

A mass minimization with stress constraints is conducted for this parameter. The objective function for mass minimization with stress constraint can be written as:

$$\min \sum m_{\theta i} \tag{4}$$

Such that:

1. $\frac{\sigma_a}{\sigma_y} \leq 0.8$
2. $\frac{\sigma_a}{\sigma_y} \leq 0.9$

where σ_a is the allowable stress in the optimization process and σ_y is the yield strength of aluminum. Two stress constraints are used here involving a maximum 80% and 90% from the yield strength.

2.2.3. Effect of Uphill Angle

The next parameter to be investigated is the uphill angle. The uphill angle variation is a representation of the uphill road which may randomly occur during cycling. In this case, three angles of 10° horizontal to 30° inclination have been used simultaneously to obtain a single topology optimization. To accommodate all of these three angles, the objective function of the compliance minimization is therefore changed into:

$$\min\left\{w_{\theta 1}\sum F_{pi}^{T}u_i + w_{\theta 2}\sum F_{pi}^{T}u_i + w_{\theta 3}\sum F_{pi}^{T}u_i\right\} \quad (5)$$

Such that: $m_{opt} \leq 0.5m_0$

where θ_1, θ_2, and θ_3 indicate the uphill angle of 10, 20, to 30°, respectively. However, since the uphill angle can be randomly different, three different cases with different weightage (w) have been used to investigate the effect of each dominant angle on the topological holes. Case 1 is designed to represent the dominance of the 10° uphill angles, while Case 2 and 3 are designed to represent the dominance of 20 and 30° uphill angles. The cases are briefly summarized in Table 2.

Table 2. Uphill angle weighting scenario.

Case	**1**			**2**			**3**		
Angle (θ)	1	2	3	1	2	3	1	2	3
	10°	20°	30°	10°	20°	30°	10°	20°	30°
Weight (w)	0.9	0.05	0.05	0.05	0.9	0.05	0.05	0.05	0.9

2.2.4. Effect of Materials

Lastly, to see the effect of different materials characteristics, two materials with different mechanical properties are used which are AL 7005 aluminum to represent the isotropic material and carbon fiber as the anisotropic material. These materials are chosen to represent the two most commonly used material in a bike crank, i.e., metal and composite. The compliance minimization with mass constraint is used to be able to compare the topological difference between the two materials with the same mass:

$$\min\sum F_{pi}^{T}u_i \quad (6)$$

Such that: $m_{opt} \leq 0.5m_0$

The properties of the materials are shown in Table 3 [27].

Table 3. Model properties.

Material	**AL 7005 Aluminum (Isotropic)**	**Carbon Fiber (Anisotropic)**
Density	2780 kg/m^3	1750 kg/m^3
Young's Modulus	71,000 MPa	-
Young's Modulus (x-direction)	-	3.95×10^{11} Pa
Young's Modulus (y-direction)	-	6×10^{9} Pa
Young's Modulus (z-direction)	-	6×10^{9} Pa
Poisson's ratio	0.33	-
Poisson's ratio (xy-direction)	-	0.2
Poisson's ratio (yz-direction)	-	0.4
Poisson's ratio (xz-direction)	-	0.2
Shear Modulus	2.67×10^{10} Pa	-
Shear Modulus (xy-direction)	-	8×10^{9} Pa
Shear Modulus (yz-direction)	-	2.14×10^{9} Pa
Shear Modulus (xz-direction)	-	8×10^{9} Pa
Ultimate Tensile Strength	280 MPa	3500 MPa

In the ANSYS environment, the carbon fiber is modeled as an anisotropic material by selecting the composite materials option in the engineering data sources. The unidirectional fiber orientation along the x-direction of the crank arm is used which means all fibers are parallel to each other.

2.3. Response Surface Optimization Method

The next optimization stage is applying the response surface optimization. This is considered as a shape optimization for the created topological shape in the previous stage. The objective function of this method is to reduce the stress that is occasionally increased due to the presence of the topological hole. The two most significant parameters from the topological result are selected as variables for shape optimization. In ANSYS Workbench environment, the 2nd order polynomial response surface can be generated by employing the design of experiment tools then followed by the response surface tools. The result of the final optimization is, eventually, presented in the form of a three-dimensional surface.

2.4. Experimental Validation

To validate the stress performance (max Von Mises stress) of the optimized bike crank arm result, an experimental study is conducted. A three-dimensional printed model is used to create the crank arm model obtained from topology optimization precisely. Three-dimensional printing is used in this research since it is the most suitable and efficient method to validate such a topology optimization model, as previously done by Li et al. [28] and Kazakis et al. [29]. The material for 3D printing is the polylactic acid (PLA) plastic which is well-known and widely used in the 3D printing field. It is also known that the PLA is not a material used to fabricate a crank arm in a real application. However, it is used in this paper since it offers an avenue to conduct a preliminary validation of the topology optimization result.

Rosette strain gauges are assembled on the crank to measure the strain after the loading. In the loading process, two different loads are applied, i.e., static and dynamic loads. The static load simply means an application of only one single load to the crank arm. This was done merely to verify the measurement method and validate the static finite element stress result. Next, the dynamic load is applied using real cycling load from a cyclist to the crank arm which has been installed on a bike. The result from the dynamic load test is a time-series data so that the maximum and minimum load during cycling can be observed and recorded.

The signal from strain gauges is processed using Arduino Nano and sent to the computer or mobile device via Bluetooth connection. Then, the signal is post-processed in the computer using Microsoft Excel to calculate the stress. The employment of Arduino Nano and Bluetooth connection is purposely to neglect the complexities of using too many and long cables during measurement that might give some analog noise to the result which can be seen from the previous study [24]. The stress data from the experiment is then compared with the simulation result from ANSYS with PLA material. Figure 6 below shows the experimental setup of the measurement.

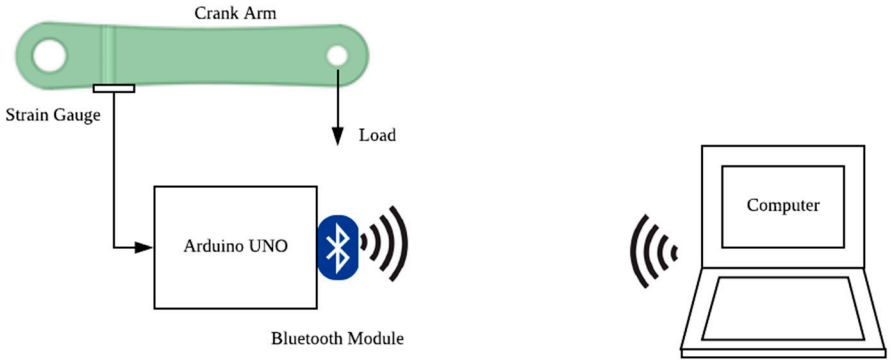

Figure 6. Experimental setup.

The obtained strain from the rosette strain gauge ε_1,ε_2,ε_3 are used to calculate the maximum shear stress and Von Mises stress using:

$$\tau_{\max} = \frac{E}{2(1+\upsilon)} \sqrt{2\left|(\varepsilon_1 - \varepsilon_3)^2 + (\varepsilon_2 - \varepsilon_3)^2\right|} \tag{7}$$

$$\sigma_{VM} = \sqrt{\sigma_{\max}^2 + \sigma_{\min}^2 - (\sigma_{\max}\sigma_{\min})} \tag{8}$$

3. Results and Discussion

3.1. Topology Optimization Result

The topology optimization history can be seen clearly in Figure 7. It shows the compliance minimization of the sample with fine mesh (967,769 nodes and 677,089 elements) showing the results from the 5th to the last 22th iteration. It costs around 150 min of computing time. The computer used in this research has the AMD Ryzen Threadripper 1950X 16-Core Processor 3.40 GHz with 32.0 GB installed RAM. The iteration shows that the optimization procedure attempts to reduce mass in the low-stress distribution are which is, in this case, located mainly in the middle of the arm and around the pedal hole. Indeed, this involves the stress result from the initial crank arm geometry that has also been already conducted in the process. This phenomenon is typical with the previous study for thin-walled structures [21]. Moreover, the center location of the crank arm also has the most homogeneous material so that the density also has similar properties. Meanwhile, both the shaft and pedal holes are retained from reduction since both holes are set to be the nondesign region. They are also the place where force is applied and fixed boundaries are implemented as mentioned before.

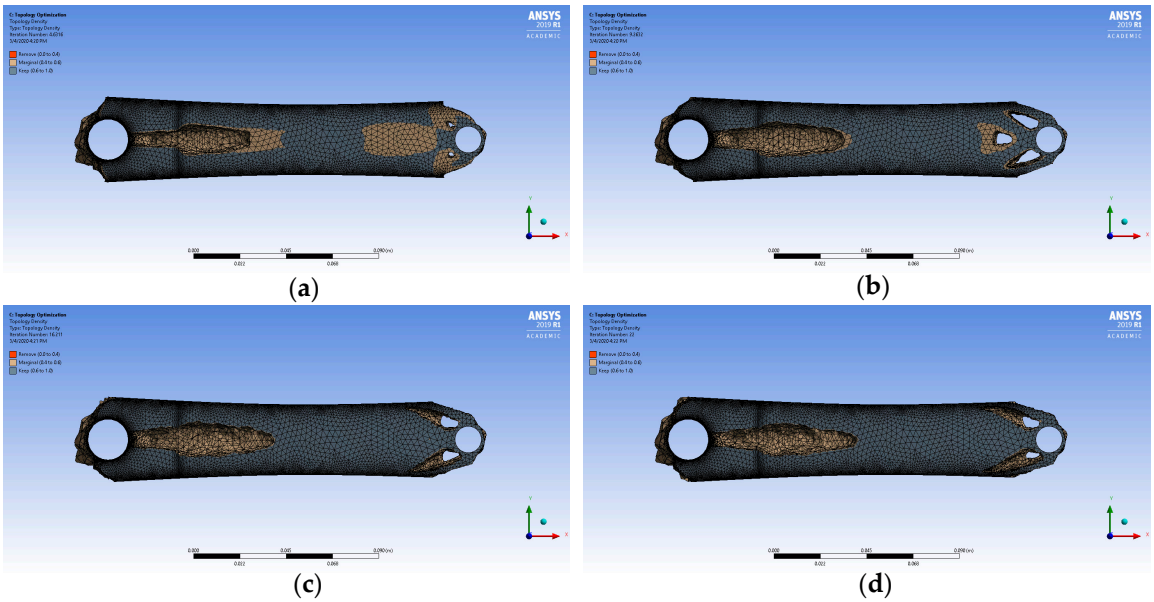

Figure 7. The topology optimization history: (**a**) 5th iteration, (**b**) 10th iteration, (**c**) 16th iteration, (**d**) 22nd iteration.

It can also be interestingly discussed that starting from the 16th iteration, the topological pattern does not considerably change. There are only slight differences in small particular sections where the effect of the changes can be considered neglected. This means that at the 16th iteration, the optimization process is nearly in steady-state condition until the 22nd iteration with neglectable changes. After that, no more pattern occurs from the optimization process. Eventually, the iteration stops at the 22nd iteration whereas the absolute steady-state optimized geometry has been achieved.

3.1.1. Geometry Creation

After the optimization has reached its steady-state condition above, the next step of the research is creating a manufacturable geometry. From Figure 7d, it can be seen that the optimized geometry is still rough and difficult to be manufactured. Therefore, the geometry should be redrawn again using CAD in the SpaceClaim software to avoid the complexity and achieve manufacturability. This process is called the geometry creation. This process involves neglectable mass elimination, curve fitting and smoothening, radius creation, as well as symmetrical aspects consideration. By considering all those aspects, the final geometry can be created, as seen in Figure 8 below.

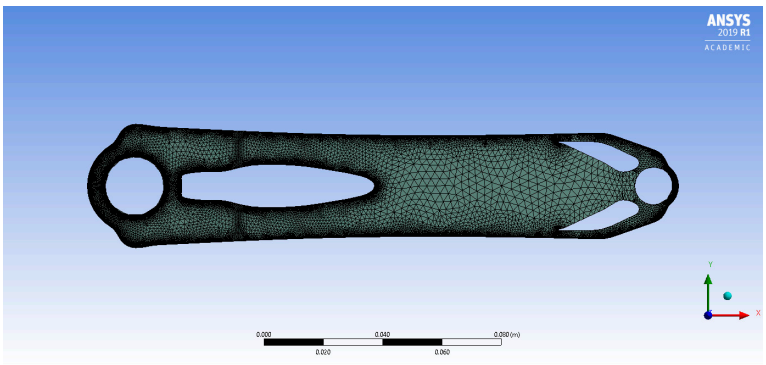

Figure 8. The final geometry of the topology optimized design.

Now, the optimized geometry has a simpler shape and less complexity. It also clearly shows that the optimization method gives significant mass reduction which is emphasized by the presence of holes on the crank arm. The holes significantly reduce the initial mass of the crank arm roughly by 0.1 kg from its original mass of 0.30 kg, which now turns into 0.2 kg. This mass reduction and holes geometry could become the basic approach for lightweight structure creation of the bike crank arm which has never been done before. It is also one of the most important aspects to be discussed since it is related closely to the stress distribution of both before and after the optimization process as the stress distribution is an envelope for all the load cases.

From the stress distribution result of the optimized design in Figure 9, it is found that the multiple loads' application on the crank arm results in nonsymmetrical stress distribution. This is caused by the direction of the multiforces that are dominantly in the negative y-direction for all given angles. Proportionally, the moment also moves towards the negative y-direction, as well. This makes the lower part of the crank arm experiencing higher compression stress than the upper part tension stress. We can also see from the result that the compression stress occurs almost throughout the lower part of the crank while the tension stress occurs only up to the middle part of the crank arm.

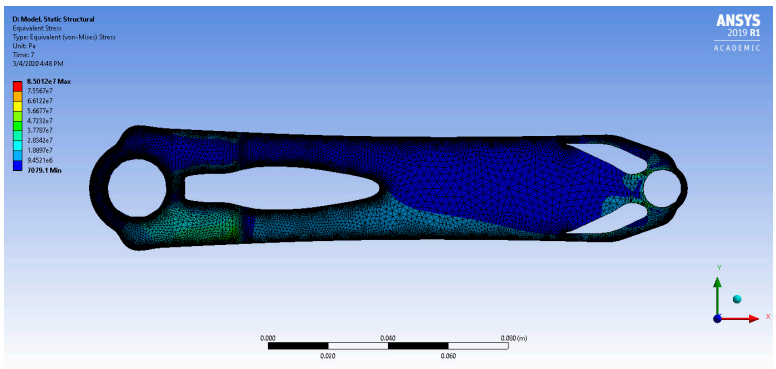

Figure 9. Stress distribution of the topology optimized design.

From the maximum stress point of view, it can be seen that the optimized design gives significant differences in von Mises stress compared to the original design. The stress has been increased from 33.2 to 85.0 MPa. Similar to the previous result from Hu et al. [20] and McEwen et al. [23] where the narrowing cross-sectional area obtained from the topological optimization hole significantly increases the stress concentration of the crank. Even though the maximum stress is increased, the value is still considerably far below the material yield strength also known as being still in the safety elastic region. Nevertheless, this will be improved by implementing the response surface optimization which will be discussed in the next section.

3.1.2. Effect of Mass Constraint

Figure 10 shows the optimization result for several mass constraints from 30% to 60% mass constraint. It can be seen that each variation gives different topological results from one another. In a more specific discussion, the hole patterns created from the minimization process are proportional to the increment of mass constraint percentage. As the mass percentage increases, the holes created on the arm reduces. It can be seen at the result of the sample with a 30% mass constraint which shows a very large hole at the center of the crank arm and several holes around the pedal holes with only a thin or narrow mass remaining at the top and bottom of the crank arm. These two conditions make a high-stress concentration level at those particular areas due to the narrowing geometry.

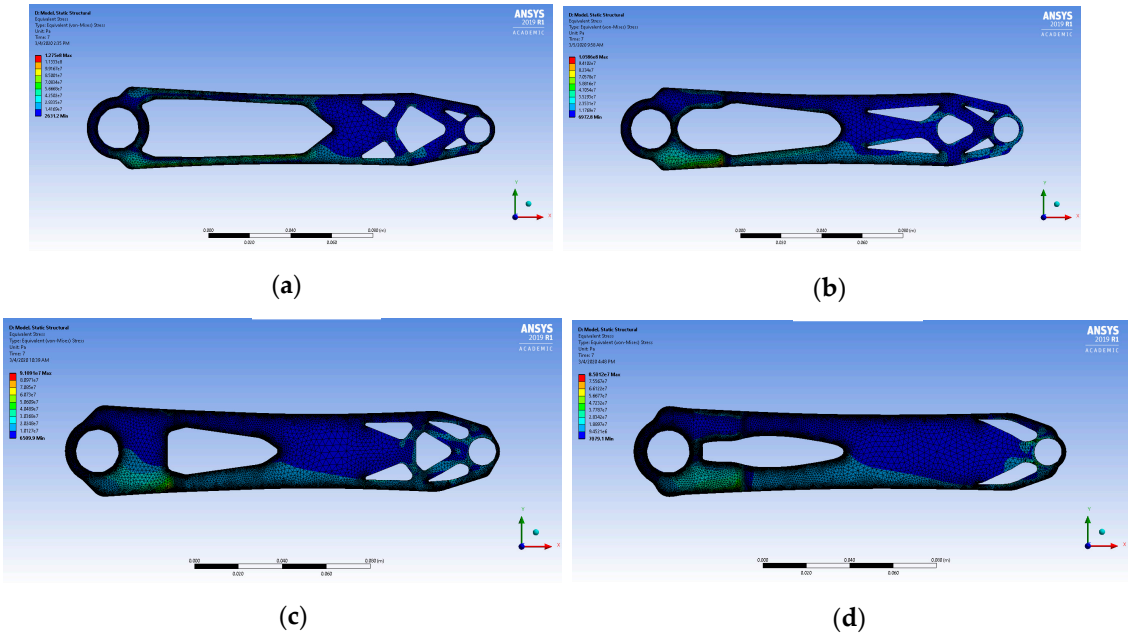

Figure 10. Effect of mass constraint in compliance minimization: (**a**) 30%, (**b**) 40%, (**c**) 50%, (**d**) 60%.

Meanwhile, the result from the sample with 40% and 50% mass constraint shows a bit similar in terms of the hole pattern. Generally, one large hole is close to the crankshaft hole and the other several holes are close to the pedal hole. However, the hole size from the sample with a 50% mass constraint is considerably smaller than that of a 40% mass constraint. On the other hand, the sample with a 40% mass constraint has more narrow areas with higher stress levels. Lastly, the result from 60% mass constraint only creates two small holes close to the pedal hole and one hole close to the crankshaft hole, respectively. Both holes are considerably smaller compared to the previous mass constraints.

From the optimized mass result, the sample with a 30% mass constraint gives 0.09 kg final mass and 127.5 MPa Von Mises stress. The sample with a 40% mass constraint gives 0.12 kg final mass and 105.8 MPa Von Mises stress. The sample with a 50% mass constraint gives 0.15 kg final mass and 91.01 MPa Von Mises stress. Lastly, the sample with a 60% mass constraint gives 0.2 kg final mass and

85.01 MPa Von Mises stress. Based on the result above, in terms of mass reduction, the optimization method seems to successfully work with the mass or volume constraints.

3.1.3. Effect of Stress Constraint

The mass optimization result with two cases of stress constraints can be seen in Figure 11. It shows the optimized crank arm with stress constraints of 80% and 90% yield strength. In terms of topological holes, the difference between the two cases is considerably small. Both have two large horizontal holes in the middle of the body and two small holes close to the pedal hole. The maximum stress obtained from both cranks is 92.0 and 133.6 MPa, respectively. The obtained stress value is lower than the constraint due to the smoothening and rounding process for the topological hole during geometry creation.

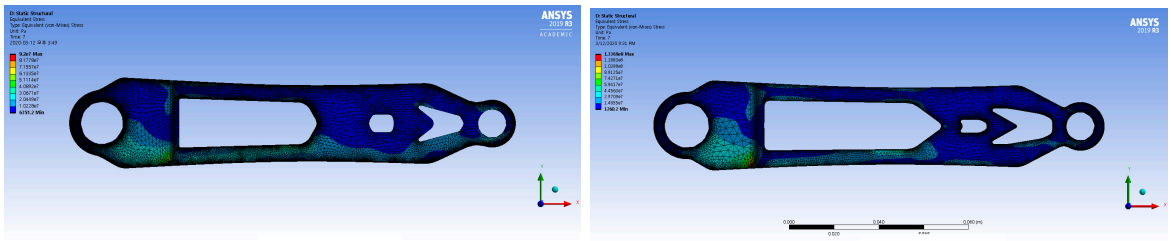

(**a**) (**b**)

Figure 11. Effect of stress constraint in mass minimization: (**a**) 80% yield strength, (**b**) 90% yield strength.

From the above two optimization parameters, i.e., compliance and mass, it is then interesting to inspect the overall optimization performance by objective functions, as well as mesh refinement. For comparison purposes, the coarse model of 48,020 elements is optimized in the same manner. In the fine model, the number of elements is 677,089, as previously indicated. Table 4 shows the compliance comparison among the selected models. This is beneficial to observe whether a coarser mesh provides a significant impact on the compliance value, as well as the topological holes pattern. The sample from compliance minimization with 50% and 60% mass constraint and sample from mass minimization with 80% and 90% stress constraint are used for observation. From the table, the sample with 50% and 60% mass constraint (compliance minimization) has similar compliance values between the coarse and fine mesh. Similarly, the sample with an 80%–90% stress constraint (mass minimization) also has identical compliance value. This shows that for those samples, even though the topological holes obtained from the optimization process is not identical (as seen in Figure 12), that does not seem to bring much different changes in the optimized compliance value or the obtained mass.

Table 4. Compliance comparison between coarse and fine mesh model.

Sample		Final Mass (kg)		Compliance (J)		Stress (MPa)	
		Coarse Mesh	Fine Mesh	Coarse Mesh	Fine Mesh	Coarse Mesh	Fine Mesh
Compliance Minimization	50% Mass constraint	0.15	0.15	0.0002	0.00021	68.27	91.09
	60% Mass constraint	0.18	0.19	0.0002	0.00021	57.63	85.01
Mass Minimization	80% Stress Constraint	0.17	0.16	0.0003	0.0003	64.8	92.0
	90% Stress Constraint	0.16	0.15	0.0007	0.00069	66.7	133.6

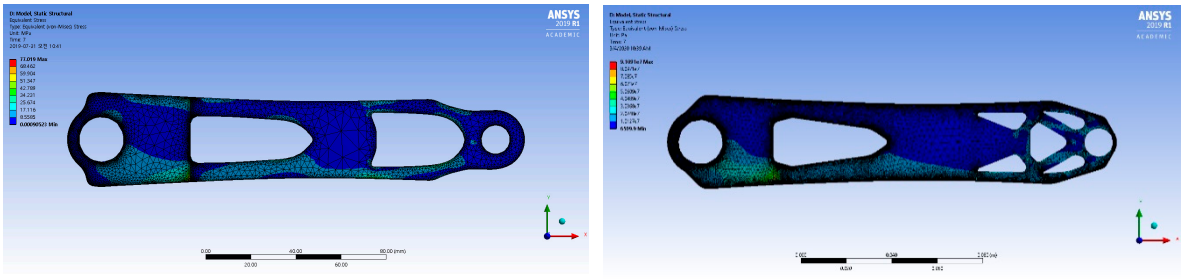

(**a**) (**b**)

Figure 12. Example of topological holes obtained with different mesh sizes (compliance minimization with 50% mass constraint): (**a**) Coarse mesh, (**b**) fine mesh.

3.1.4. Effect of Uphill Angle

The result of each angle of domination for compliance minimization can be seen in Figure 13. It is seen that the uphill angle gives a direct visible impact to the topological hole symmetry. As the uphill angle domination increases, the generated topological holes become more asymmetric particularly at the top region of the crank arm. Proportionally, in terms of stress distribution, it also shows a similar pattern with the result of the holes. The uphill angle increment makes the stress distribution to be distributed unevenly throughout the body caused by the asymmetrical aspects. This, in turn, also creates higher stress compared to the mass constraint variation. This result is linear with the report from Bouillod et al. [30] that shows the increment of cycling force during the uphill track, as well as the energy consumption in the cyclist body.

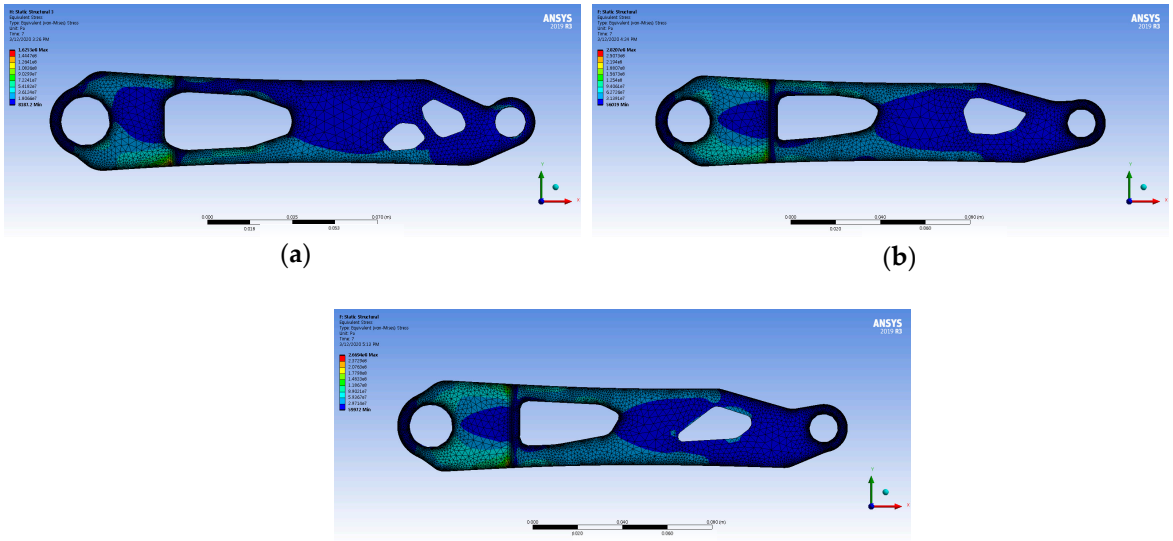

(**a**) (**b**)

(**c**)

Figure 13. Effect of uphill angle (compliance minimization): (**a**) Case 1, (**b**) Case 2, (**c**) Case 3.

3.1.5. Effect of Materials

Figure 14 shows the result of the material property's effect, i.e., isotropic and anisotropic properties on the topological optimization pattern. The topological result between the two materials is significantly different from each other. As the result of the aluminum, the crank arm has been discussed before in the previous subsection. Here, the result from the anisotropic carbon fiber crank arm is interesting to be discussed. It is seen that instead of having two general topological holes, it only has one large triangular-like hole in the middle of the body of the crank arm.

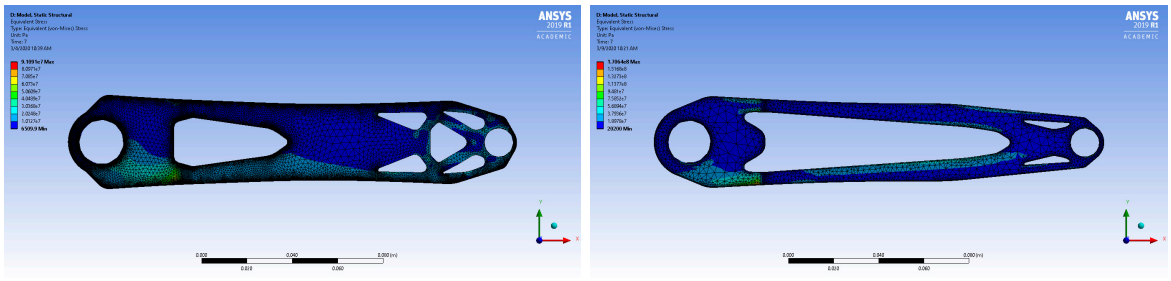

(**a**) (**b**)

Figure 14. Effect of material: (**a**) Aluminum alloy, (**b**) carbon fiber.

As known before, the aluminum crank arm here has the common solid isotropic where the value of Poisson's ratio is constant at each three-dimensional x, y, and z-direction. Meanwhile, the Poisson's ratio of the anisotropic materials differs along those three-axis. In Table 2, it is seen that the Poisson's ratio of the carbon fiber is different in each direction, i.e., 0.2, 0.4, and 0.2 for XY, YZ, and XZ direction, respectively. This, in turn, makes the stress distribution along the axis to also differ. From Figure 14, we can see that the stress distribution is quite different between the two and, therefore, the topological hole created based on the stress distribution is also different. This phenomenon has been discussed by Farhan et al. [31] which investigates the stresses of a nonhomogeneous composite material that shows the asymmetric behavior of the mechanical properties.

3.2. Response Surface Optimization

From all the variation results by topology optimization, in general, there are two topological holes obtained for all the models. These holes create narrow shapes for the crank arm which consequently creates a high-stress concentration region (red circle) particularly from the bigger hole close to the crankshaft. Therefore, to improve this weakness, a response surface optimization method is implemented. This method can be considered as shape optimization. Two research variables have been chosen, i.e., the two topological holes from the simplified optimized crank arm, as seen more in Figure 15 as follows:

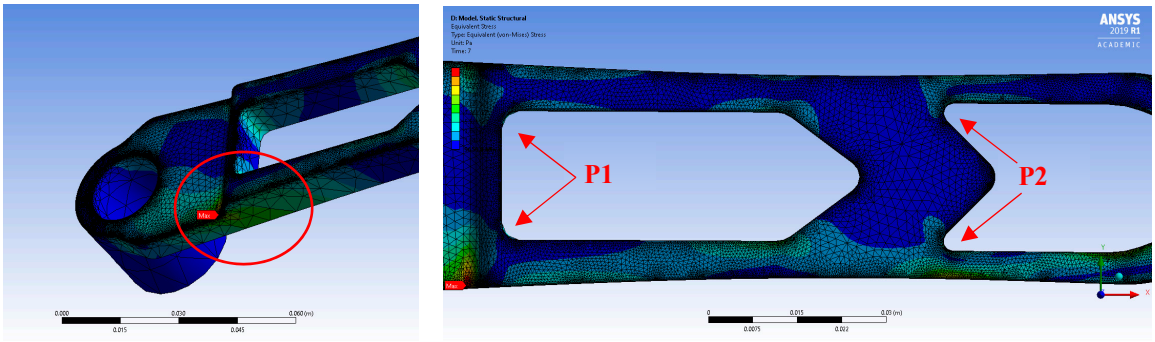

Figure 15. Two topological radius P1 and P2 as the response surface optimization variables.

The first hole radius near the crankshaft hole is assigned as P1 or the first variable while the hole radius near the pedal hole is P2, respectively. Each of these two variables is then varied in terms of radius increment from 0 to 5 mm and investigated following a design of experiment procedure in the ANSYS Response Surface Optimization Software (RSM) to obtain the optimum result. Figure 16 shows an example of how this radius evolves.

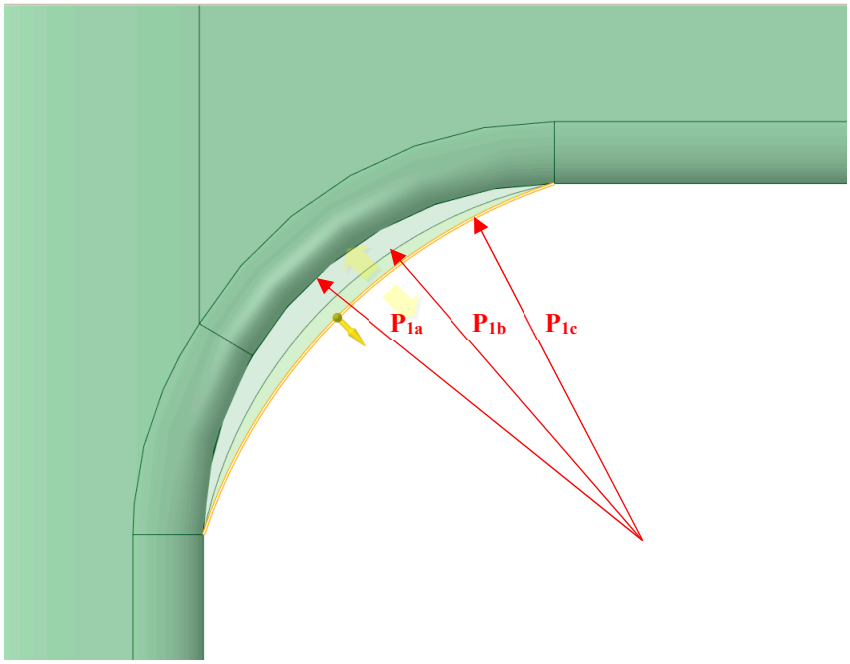

Figure 16. Example of how radius P1 evolves from P1a to P1c during the response surface optimization.

The objective function for this process is stress minimization as discussed before. Then, the software makes sufficient iteration at near the optimum value to get the final minimum stress result. The result of the RSM process is presented in the surface-like graph which can be seen in Figure 17. In this case, the minimum point for P1 and P2 are obtained at 4.75 and 1.25 mm. This means that the best increment for both hole radiuses is 4.75 mm for the hole near crankshaft and 1.25 mm for the hole near the pedal. This method is implemented in all the samples and results in the data presented in Table 5. It shows the final maximum stress and the percentage of reduction after the response surface method is implemented.

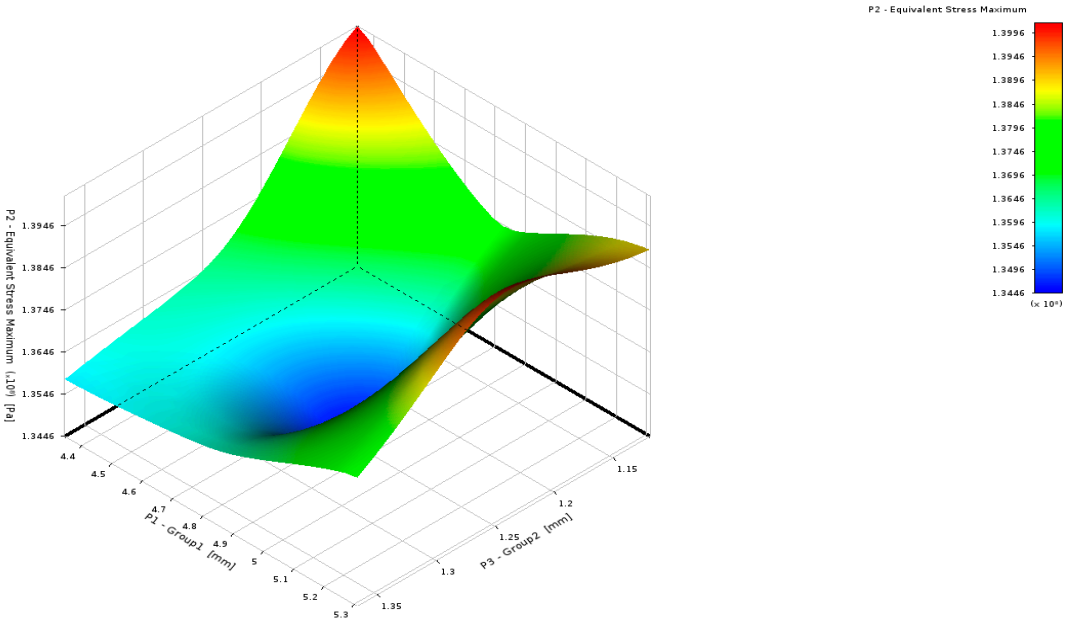

Figure 17. Response surface optimization result.

Table 5. Maximum equation Von Mises stress comparison.

Sample		Topology Optimization (MPa)	Response Surface Method (MPa)	Reduction (%)
Compliance Minimization	30% Mass constraint	127.5	126.4	0.80
	40% Mass constraint	105.8	105.7	0.10
	50% Mass constraint	91.09	71.2	21.8
	60% Mass constraint	85.01	71.4	16.0
Mass Minimization	80% Stress Constraint	92.0	87.2	5.21
	90% Stress Constraint	133.6	133.3	0.22
Compliance Minimization	Uphill Angle Case 1	101.3	99.9	1.38
	Uphill Angle Case 2	115.9	113.9	1.72
	Uphill Angle Case 3	124.3	120.3	3.21
	Carbon Fiber	187.8	186.2	0.85

To improve the stress performance of the optimized crank arm, we applied the response surface optimization for all cases by topology optimization as summarized in Table 5. All the maximum stress of the crank arm has been successfully improved from their previous topology optimization result. The highest reduction is obtained by the 50% mass constraint crank arm with a 21.8% reduction. This once again, shows that increasing the hole radius by only around 0–2 mm will make significant differences to the obtained stress. Meanwhile, the lowest reduction is obtained by the 40% mass constraint with only 0.1%. However, an improvement still can be obtained using the RSM method.

As a conclusion for this section, the newly optimized crank arm provides at least three benefits. First, the optimized geometry has a significantly lower mass than the original design which can be the basis of lightweight structures. The materials for the crank arm can be variously chosen depending on the cost consideration. In other words, this optimized crank arm design can reduce the manufacturing cost. Second, the stress distribution throughout the optimized crank arm is still considered safe. It is shown by the maximum stress value that it is much lower than the yield and tensile strength for all samples. Third, this optimized design provides a more aesthetic design compared to the solid-conventionally designed original crank arm. The aesthetic issue, as we know, can be a very sensitive matter to the customers.

3.3. Experimental Validation

Figure 18a below shows the three-dimensional model result from 3D printing. The model is taken from the optimization result (Figure 12a, coarse model, compliance minimization by 50% mass constraint). This model has a similar performance to the fine mesh model in terms of the value of compliance and also offers the simplest fabrication to avoid geometry limitation in the 3D printing process. The geometrical result from the 3D printing is quite precise and acceptable, yet, the surface roughness might have a little difference with the CAD model due to the PLA fiber fabrication process. The effect of the surface roughness is, therefore, excluded from the discussion. However, during strain gauge placement, the surface has been smoothened by using sandpapers to avoid noise and measurement bias due to roughness issue.

(**a**)

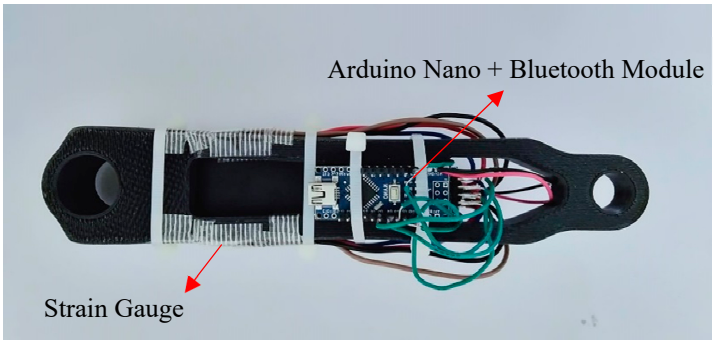

(**b**)

Figure 18. (**a**) Three-dimensional (3D) printing result, (**b**) strain gauge, and Arduino installation.

Figure 18b shows the strain gauge installment on the crank arm, as well as the Arduino Nano package. The placement of the strain gauge follows the maximum stress resulting from the simulation result, as discussed in the previous subsection. It has been known that it is located at the bottom of the narrow section of the topological hole near the crankshaft hole. In order to be able to read the stress data more accurately, the strain gauges are placed using the Rosette arrangement, as seen in Figure 19.

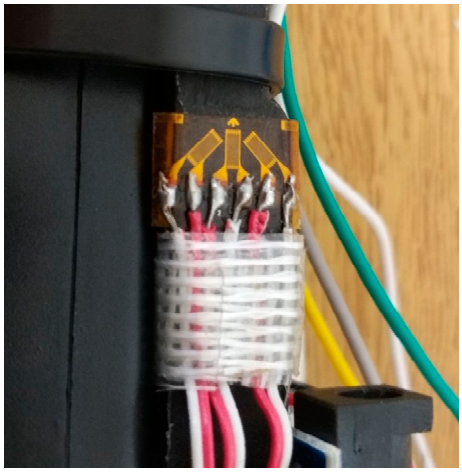

Figure 19. The Rossette strain gauge.

From the figure, it is seen that this arrangement provides a simpler and tidier measurement compared to the previous work [24] since only less electric cables are involved. Moreover, the wireless connection provides a more effective and convenient procedure for both static and dynamic measurements. The validation process is conducted using 1 kg weight as a static load given to the crank arm in the horizontal (0°) position. The crankshaft is set to be fixed at this position so that

the stress data from the strain gauge can be processed by the Arduino Nano. This measured data is then compared with the result from ANSYS simulation using the same static load of 1 kg weight.

The strain gauge measurement has been calibrated before the experiment that the static test is conducted to ensure the experimental process. The measurement time is conducted for about 1 min to get a steady-state reading from the strain gauge. The obtained stress range is between 0.983 to 0.989 MPa. For clearer observation, Figure 20 shows the overall result of the static test result from 0 to 70 s. If we take an average of this stress as 0.98 MPa, the percentage error between simulation and experimental result is only around 8% as provided in Table 6. Therefore, it can be said that both simulation and static validation experiment shows considerable agreement and can be validly used for further investigation.

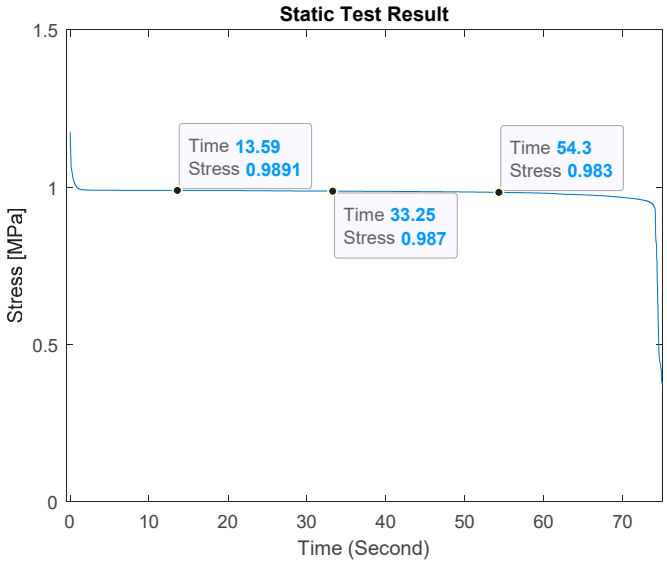

Figure 20. Static test result.

Table 6. Static stress validation measurement.

ANSYS Simulation (MPa)	Static Load Experiment (MPa)	% Error
1.078	0.98	8.4

In order to enhance the discussion, the dynamic test result has also been obtained. Figure 21 shows the experimental procedure of the dynamic experiment. The bicycle is installed on a bicycle treadmill stand and a cyclist rides the bicycle as usual. The cycling load is obtained from the cyclist's foot during cycling in a low gear position. The average cycling speed is set to be 1 cycle/s or 60 rotations/min.

Two types of cycling loads are applied. First, the load is applied only to the optimized crank arm which is placed on the left side of the crank as seen in the figure. The right-hand side crank arm is left to be rotated by itself without any load applied. The result of this experiment is shown in Figure 22 below. It is clearly seen that the stress value oscillates along the cycling period which indicates the maximum and the minimum stress value. Three maximum (peak) stresses indicated in the figure show the value of 2.31, 2.36, and 2.46 MPa, respectively. This also indicates that the multiple loads used in the simulation considerably match with practical situations and are possibly used for future dynamic investigation.

Figure 21. Dynamic load experiment.

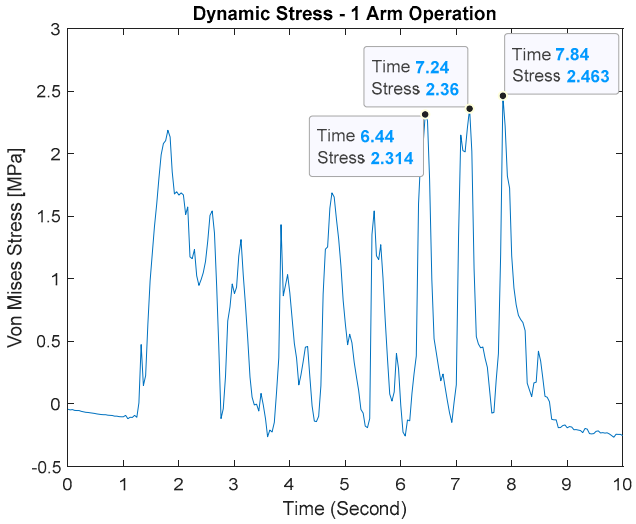

Figure 22. Dynamic test result (single crank arm operation).

The second type is the application of cycling load on both the left side (optimized) and right-hand crank arm. Now, the stress results considerably change in order to be multiplied since the crank arm suffers the cycling force from both pedals (see Figure 23). However, this inertial negative value from the other pedaling force is neglected here and our focus is merely on the pure positive pedaling force on the optimized crank arm. Even so, the maximum stress value indicated by the three-peak points in the figure shows a multiplying higher value. The maximum stress is 12.89, 12.91, and 13.46 MPa, respectively. It clearly indicates that the pedaling force gives a significant effect on the bike crank arm and plays a major role in cycling dynamics.

For comparison, the experimental result of one arm operation from Ramos et al. [32] is plotted together with the author's present result in Figure 24. The maximum stress peak of the author obtained in Figure 22 at around 7 sec is replotted again in the form of a crank angle position by dividing one cycle experimental data into 0–180° angle evenly. Here, a normalized Von Mises stress is used in order to make an *apple-to-apple* comparison between the two experiments since the experimental environment is not identical between each other. However, the comparison still can be made based on the normalized value to provide some useful insight. From Ramos' results, the maximum cycling force occurs at around 60 to 120° crank angles shown by the stress peak at a 90° angle. While the author's result peak is obtained at the 120° angle. Even though the maximum stress from the author

has a different position compared to Ramos et al.'s result, it can be seen that the overall Von Mises stress distribution has a similar pattern. This similarity does not only indicate that the present measurement procedure is considered acceptable, but also indicates the benefit of the optimized crank arm geometry. With considerably lesser mass and lighter material, it can provide similar performance with the conventional crank arm design. It can even be improved by choosing other materials with higher mechanical properties.

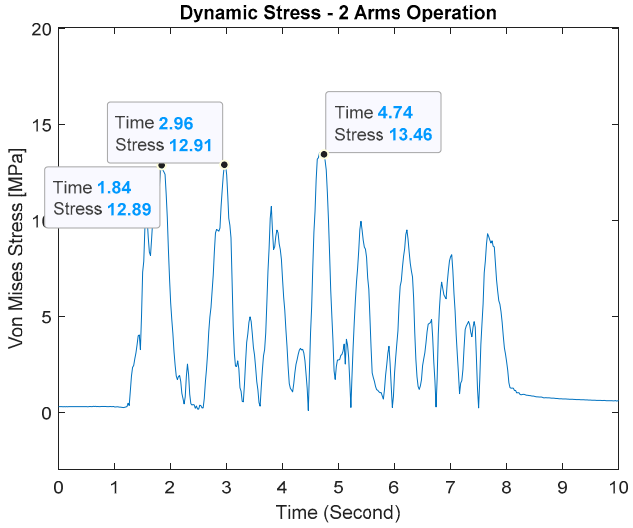

Figure 23. Dynamic test result (double crank arms operation).

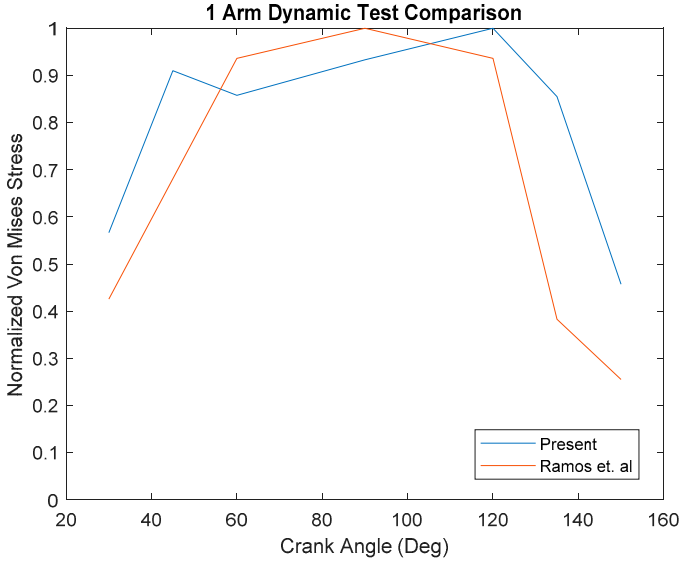

Figure 24. Normalized Von Mises stress comparison to Ramos et al. [32].

4. Conclusions

In this paper, topology and response surface optimization methods have been applied to a bicycle crank arm with multiple load conditions. Several scenarios of mass minimization have been investigated resulting in several optimized crank arm designs. The following conclusions are obtained:

1. The topology optimization successfully provides structural mass reduction up to 70% from the initial mass. This is a very effective way to create a lightweight structure that is important in the development of future bicycle design. From several constraint investigations, the topology

optimization method is also capable of providing many geometrical options for the design of a lightweight crank arm.

2. The response surface method is also found to be effective as a shape optimization tool for this crank arm case. It is able to enhance the stress level performance of the optimized crank arm obtained from topology optimization.
3. The optimized model has been validated by static and dynamic experiments which shows a very well agreement. A comparison study with the previous conventional bike crank arm design shows that the optimized geometry, with less mass, can give a similar performance and possibly be improved in the future.
4. Improvement opportunities can be made in the future involving more detail of dynamic analysis and experimental studies, i.e., speed variations and road conditions to enhance the application of the crank arm in some particular application, i.e., hybrid and electric bicycle.

In summary, the topology and response surface optimization are the effective combination tools for the bicycle crank arm design optimization.

Author Contributions: Conceptualization, A.Y.I. and B.K.; methodology, A.Y.I. and B.K.; software, B.K.; validation, A.Y.I. and B.K.; formal analysis, A.Y.I. and B.K.; investigation, A.Y.I., G.N., and B.K.; resources, A.Y.I. and B.K.; data curation, A.Y.I. and G.N.; experiment, A.Y.I. and N.T.; writing—original draft preparation, A.Y.I.; writing—review and editing, B.K.; visualization, A.Y.I. and B.K.; supervision, B.K.; project administration, B.K.; funding acquisition, B.K. All authors have read and agreed to the published version of the manuscript.

Funding: This work was supported by the National Research Foundation of Korea (NRF) grant by the Korea government (no. NRF-2018R1D1A1B07050370) and the Human Resources Development Program (grant no. 20194010201800) of the Korea Institute of Energy Technology Evaluation and Planning (KETEP) grants by the Korea government.

Conflicts of Interest: The authors declare no conflict of interest.

References

1. Höchli, B.; Brügger, A.; Abegglen, R.; Messner, C. Using a goal theoretical perspective to reduce negative and promote positive spillover after a bike-to-work campaign. *Front. Psychol.* **2019**, *10*, 433. [CrossRef] [PubMed]
2. Shin, H.C.; Kim, D.; Lee, J.Y.; Park, J.; Jeong, S.Y. *Bicycle Transport Policy in Korea*; Korea Transport Institute: Geumnam-myeon, Korean, 2013.
3. ISO. *International Standard ISO and Safety Requirements for Systems and Components Used on Machinery as Defined*; ISO: Geneve, Switzerland, 2010; Volume 2010.
4. Sena Cardoso, F.; Rasmussen, K.J.R.; Zhang, H. System reliability-based criteria for the design of steel storage rack frames by advanced analysis: Part I—Statistical characterisation of system strength. *Thin-Walled Struct.* **2019**, *141*, 713–724. [CrossRef]
5. Dai, W.; Chi, Y.; Lu, Z.; Wang, M.; Zhao, Y. Research on reliability assessment of mechanical equipment based on the performance-feature model. *Appl. Sci.* **2018**, *8*, 1619. [CrossRef]
6. Batchelder, J.S.; Crump, S.S. Method for Rapid Prototyping of Solid Models. U.S. Patent 5866058, 2 February 1999. Available online: https://patents.google.com/patent/US5866058A/en (accessed on 3 April 2019).
7. Edwards, C.H. Light-Weight Bicycle Crankshaft Assembly Utilizing Two-Piece Axle Integrally Joined to Crank Arms. U.S. Patent 5493937, 27 February 1996.
8. Zamparo, P.; Minetti, A.E.; Di Prampero, P.E. Mechanical efficiency of cycling with a new developed pedal-crank. *J. Biomech.* **2002**, *35*, 1387–1398. [CrossRef]
9. Bendose, M.P.; Sigmund, O. *Toplogy Optimization, Theory, Methods and Applications*; Springer: Berlin, Germany, 2003.
10. Yang, D.; Liu, H.; Zhang, W.; Li, S. Stress-constrained topology optimization based on maximum stress measures. *Comput. Struct.* **2018**, *198*, 23–39. [CrossRef]
11. Viviani, A.; Iuspa, L.; Aprovitola, A. Multi-objective optimization for re-entry spacecraft conceptual design using a free-form shape generator. *Aerosp. Sci. Technol.* **2017**, *71*, 312–324. [CrossRef]
12. Zhang, P.; Xu, Y.; Le, C.; Ding, H.; Guo, Y. Structural Optimization Method for the Transition Section in Composite Bucket Foundations of Offshore Wind Turbines. *Energies* **2018**, *11*, 3230. [CrossRef]

13. Slavov, S.; Konsulova-Bakalova, M. Optimizing Weight of Housing Elements of Two-stage Reducer by Using the Topology Management Optimization Capabilities Integrated in SOLIDWORKS: A Case Study. *Machines* **2019**, *7*, 9. [CrossRef]
14. Orme, M.; Madera, I.; Gschweitl, M.; Ferrari, M. Topology Optimization for Additive Manufacturing as an Enabler for Light Weight Flight Hardware. *Designs* **2018**, *2*, 51. [CrossRef]
15. Qu, Y.; Jiang, Y.; Feng, L.; Li, X.; Liu, B.; Wang, W. Lightweight Design of Multi-Objective Topology for a Large-Aperture Space Mirror. *Appl. Sci.* **2018**, *8*, 2259. [CrossRef]
16. Sleesongsom, S.; Bureerat, S. Topology Optimisation Using MPBILs and Multi-Grid Ground Element. *Appl. Sci.* **2018**, *8*, 271. [CrossRef]
17. Frascolla, V.; Dominicini, C.K.; Paiva, M.H.M.; Caporossi, G.; Marotta, M.; Riberio, M.R.N.; Segatto, M.E.V.; Martenillo, M.; Monteiro, M.E.; Both, C.B. Optimizing C-RAN Backhaul Topologies: A Resilience-Oriented Approach Using Graph Invariants. *Appl. Sci.* **2019**, *9*, 136. [CrossRef]
18. Tauzowski, P.; Blachowski, B.; Lógó, J. Advances in Engineering Software Functor-oriented topology optimization of elasto-plastic structures. *Adv. Eng. Softw.* **2019**, *135*, 102690. [CrossRef]
19. Pinskier, J.; Shirinzadeh, B. Topology optimization of leaf flexures to maximize in-plane to out-of-plane compliance ratio. *Precis. Eng.* **2019**, *55*, 397–407. [CrossRef]
20. Hu, Z.; Gadipudi, V.K.; Salem, D.R. Topology Optimization of Lightweight Lattice Structural Composites Inspired by Cuttlefish Bone. *Appl. Compos. Mater.* **2019**, *26*, 15–27. [CrossRef]
21. Tsavdaridis, K.D.; Efthymiou, E.; Adugu, A.; Hughes, J.A.; Grekavicius, L. Application of structural topology optimisation in aluminium cross-sectional design. *Thin Walled Struct.* **2019**, *139*, 372–388. [CrossRef]
22. Jewett, J.L.; Carstensen, J.V. Topology-optimized design, construction and experimental evaluation of concrete beams. *Autom. Constr.* **2019**, *102*, 59–67. [CrossRef]
23. McEwen, I.; Cooper, D.; Warnett, J.; Kourra, N.; Williams, M.; Gibbons, G. Design & Manufacture of a High-Performance Bicycle Crank by Additive Manufacturing. *Appl. Sci.* **2018**, *8*, 1360.
24. Casas, O.V.; Dalazen, R.; Balbinot, A. 3D load cell for measure force in a bicycle crank. *Meas. J. Int. Meas. Confed.* **2016**, *93*, 189–201. [CrossRef]
25. Sung, J.; Ba Hung, N.; Yoon, S.; Lim, O. A study of the dynamic characteristics and required power of an electric bicycle equipped with a semi-automatic transmission. *Energy Procedia* **2017**, *142*, 2057–2064. [CrossRef]
26. Ba Hung, N.; Lim, O. The effects of operating conditions and structural parameters on the dynamic, electric consumption and power generation characteristics of an electric assisted bicycle. *Appl. Energy* **2019**, *247*, 285–296. [CrossRef]
27. Minus, M.L.; Kumar, S. The processing, properties, and structure of carbon fibers. *JOM* **2005**, *57*, 52–58. [CrossRef]
28. Li, Q.; Xu, R.; Liu, J.; Liu, S.; Zhang, S. Topology optimization design of multi-scale structures with alterable microstructural length-width ratios. *Compos. Struct.* **2019**, *230*, 111454. [CrossRef]
29. Kazakis, G.; Kanellopoulos, I.; Sotiropoulos, S.; Lagaros, N.D. Topology optimization aided structural design: Interpretation, computational aspects and 3D printing. *Heliyon* **2017**, *3*, e00431. [CrossRef]
30. Bouillod, A.; Pinot, J.; Valade, A.; Cassirame, J.; Soto-Romero, G.; Grappe, F. Influence of standing position on mechanical and energy costs in uphill cycling. *J. Biomech.* **2018**, *72*, 99–105. [CrossRef]
31. Farhan, A.M.; Abd-Alla, A.M.; Khder, M.A. On problem of the stresses in a non-homogeneous composite of an infinite cylinder of orthotropic material. *Results Appl. Math.* **2019**, *3*, 100014. [CrossRef]
32. Ramos, J.A.C.; lvarez-Caldas, C.; Quesada, A.; Román, J.L.S. Determining the Stress Distribution in a Bicycle Crank Under In-Service Loads. *Exp. Tech.* **2016**, *40*, 885–890. [CrossRef]